Received: 12 January 2022 | Revised: 6 May 2022 | Accepted: 1 June 2022

DOI: 10.1111/jace.18626

Journal of the American Ceramic Society

RESEARCH ARTICLE

Sintering and foaming of bioactive glasses

Carsten Blaeß | **Ralf Müller**

Department 5 Materials Engineering, Bundesanstalt für Materialforschung und -prüfung (BAM), Berlin, Germany

Correspondence
Carsten Blaeß, Bundesanstalt für Materialforschung und -prüfung (BAM), Richard-Willstätter-Straße 11, 12489 Berlin, Germany.
Email: carsten.blaess@bam.de

Funding information
Deutsche Forschungsgemeinschaft DFG, Grant/Award Number: Mu963 18-1

[Correction added on 8th July 2022, after first online publication: The department name in affiliation of author was corrected from "Department 5.6 Glass" to "Department 5 Materials Engineering"].

Abstract

Sintering, crystallization, and foaming of 44.8SiO_2–2.5P_2O_3–36.5CaO–6.6Na_2O–6.6K_2O–3.0CaF_2 (F3) and 54.6SiO_2–1.7P_2O_3–22.1CaO–6.0Na_2O–7.9K_2O–7.7MgO (13–93) bioactive glass powders milled in isopropanol and CO_2 were studied via heating microscopy, differential thermal analysis, vacuum hot extraction (VHE), Infrared spectroscopy, and time-of-flight secondary ion mass spectrometry. Full densification was reached in any case and followed by significant foaming. VHE studies show that foaming is driven by carbon gases and carbonates were detected by Infrared spectroscopy to provide the major foaming source. Carbonates could be detected even after heating to 750°C, which hints on a thermally very stable species or mechanical trapping. Otherwise, dark gray compact colors for milling in isopropanol indicate the presence of residual carbon as well. Its significant contribution to foaming, however, could not be proved and might be limited by the diffusivity of oxygen needed for carbon oxidation to carbon gas.

KEYWORDS
bioactive glass, crystallization, foaming, sintering

1 | INTRODUCTION

The manufacturing of sintered glasses and glass–ceramics can be complicated by gas bubble formation. Unlike desired foaming,[1–5] such non-desired foaming is rarely studied, making it difficult to derive foaming mitigation strategies. Several foaming sources, like glass volatilization[6] and adsorbed water and oxygen,[7,8] crystallization-induced density change and related gas release phenomena,[9] over-firing,[10] and encapsulated sintering atmosphere[11] were discussed. Agea et al.[12] found strong effects of powder processing on foaming of commercial Ba alumino-borosilicate glass powders for solid oxide fuel cell (SOFC) sealing. The authors found that dry milling in CO_2 atmosphere increases foaming intensity dramatically compared to milling in air, Ar, N_2, or water and concluded that carbonaceous species trapped at the glass surface during milling or later storage provide the major foaming source.

This latter conclusion is consistent with other studies. Thus, it was found that freshly fractured glass surfaces can instantly trap atmospheric CO_2[13] from which a wide variety of thermally stable carbonaceous species like carboxylates, oxalates, or carbonates can emerge.[14–16] In a similar sense, Kalinkin et al.[17,18] demonstrated that intensive milling of Ca and Mg silicate minerals can cause substantial CO_2 uptake. Beyond the thermal stability of carbonaceous surface species, mechanosorption phenomena like the appearance and migration of structural defects, and plastic deformation and deformation mixing of system components,[19] propagating micro- and sub-micro-cracks or the bulk penetration of CO_2[20] have been

discussed as trapping mechanisms. In a recent study on the glass used in Ref. [12], such burying-like trapping mechanisms were indicated by the presence of molecular CO_2 unable to rotate, their large thermal stability, and the occurrence of diffusion-limited carbon gas effusion peaks close to the glass transition temperature.[21]

As for glass sealants, non-desired foaming may also occur for bioactive glasses because of their high network former content needed to ensure large degradation rates in aqueous solution. As a high network former content also increases the glass crystallization tendency, its effect on foaming is also important.

The aim of this work was to study the non-desired foaming of bioactive glasses focusing on potential foaming sources, and the effects of glass powder processing and crystallization because such basic knowledge is required for deriving mitigation strategies. Two bioactive glasses of different crystallization tendencies have been therefore considered. The fluoride-containing glass under study, F3, allows fiber drawing and sintering to dense compacts[22–24] but densification is closely followed by $Na_2CaSi_2O_6$ (combeite) crystallization.[24] The other glass, 13–93, undergoes only weak crystallization of $CaSiO_3$ (wollastonite).[24–26] To check whether CO_2 uptake during milling provides the major source of non-desired foaming as previously discussed in Refs. [12, 21] for borosilicate glass, prolonged dry milling in CO_2 atmosphere was compared with wet milling in isopropanol, as water-free milling of bioactive glasses is widely used to minimize glass corrosion.

2 | SAMPLES AND METHODS

Glasses of nominal composition $44.8SiO_2$–$2.5P_2O_3$–$36.5CaO$–$6.6Na_2O$–$6.6K_2O$–$3.0CaF_2$ (F3) and $54.6SiO_2$–$1.7P_2O_3$–$22.1CaO$–$6.0Na_2O$–$7.9K_2O$–$7.7MgO$ (13–93)[24] were prepared from reagent grade SiO_2, $CaCO_3$ (≥99% purity; Merck, Darmstadt, Germany), $NaPO_3$, Na_2CO_3, K_2CO_3, $MgCO_3$, and CaF_2 raw materials. Batches of 200 g were molten in 200-ml Pt crucibles for 1 h at 1350°C. Glass frits were produced by quenching in water. Bulk samples were casted into copper molds.

Glass powders were made by crushing and milling. After drying in air at 120°C, steel mortar crushed glass frits were sieved to 315–3150 μm and used for subsequent planetary ball milling in 80-ml zirconia jars with 10 Ø 15-mm zirconia balls per jar at 320 r/min (Pulverisette 5/2; Fritsch, Idar-Oberstein, Germany). Wet milling was done in badges of 20 g in ≈20-ml isopropanol for 10 min at 340 r/min ($F3_{Iso}$ and $13–93_{Iso}$). Wet milled powders were dried at room temperature for 16 h and then annealed at 80°C for 30 min to evaporate residual isopropanol. For dry milling in CO_2 atmosphere a planetary ball micro mill (PULVERISETTE 7, Fritsch, Idar-Oberstein, Germany) with sealed corundum jars of 25 ml, each containing seven Ø 12-mm corundum balls were used. Milling of 7-g glass per jar was done at a maximum motor speed of 3400 r/min for 60 min ($F3_{CO_2}$ and $13–93_{CO_2}$) and 120 min ($F3_{CO_{2-b}}$) in steps of 15 min with 30 min of cooling in between. For milling in CO_2, sealed jars were evacuated to <10 mbar and refilled with CO_2 (99.99%, Air Liquide, Germany) to ≈1 bar. Evacuation and gas filling were repeated five times to minimize the amount of residual air. Every 30 min, the atmosphere was renewed following the previously mentioned procedure. Glass powders were then stored in a desiccator in vacuum, which was twice evacuated and refilled with pure argon after inserting the samples. This procedure should prevent any substantial CO_2 uptake during storage.

Particle size distribution was characterized by light scattering (Mastersizer; Malvern, Worcestershire, UK) of 10 mg dispersed glass powder in a 0.003-M $Na_4P_2O_7$ solution.

Glass transition temperature and crystallization behavior was monitored by differential thermal analysis (DTA) within 5 K accuracy on 12–17-mg powder samples heated at 10 K/min using a thermobalance TAG24 (Setaram, Caluire, France).

Sintering was studied on cylindrical powder compacts uniaxially pressed at 50 MPa twice for 30 s with a break of 10 s in between. Compacts with a diameter of 5 mm, a height of ≈5 mm, and relative green densities of 55%–60% were heated up at 10 K/min on zirconia substrates (CeramTec, Plochingen, Germany) in a heating microscope (Erhitzungsmikroskop, Leitz, Wetzlar, Germany). The sample temperature was measured with 5-K accuracy.

The *relative density* of powder compacts ($\Delta\rho_{rel} = 1.3\%$) was calculated from sample mass, bulk glass density, and compact volume estimated from the compact silhouette area assuming ideal cylindrical shape according to Ref. [27].

Microstructure evolution was studied on powder compacts heated at 10 K/min to selected temperatures using the heating microscope, quenched in ambient air, and manually fractured. Fracture surfaces were studied with environmental scanning electron microscopy (ESEM) (ESEM-FEG; Philips-XL 30, Eindhoven, Netherlands) at 15 and 20 kV, respectively, and at 0.2–0.5-torr H_2 atmosphere.

Heated and quenched powder compacts were studied by means of Fourier-transformed infrared spectroscopy with attenuated total reflection ATR-FTIR in the range of 525–1700 cm^{-1} (Nicolet Avatar 370DTGS with Smart Orbit addition; Thermo Electron Corporation, Waltham, Massachusetts, USA). Measured absorbance was normalized on the maximum glass band (Si–O vibration) for each curve with calibration against air before measuring. For

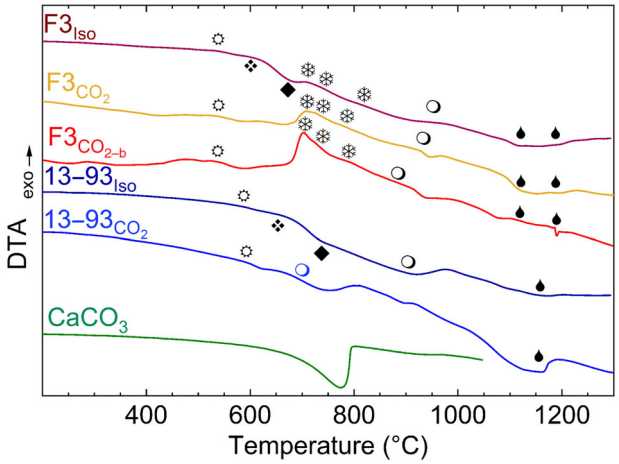

FIGURE 1 DTA curves F3 and 13–93 milled 10 min in isopropanol and 1 h in CO_2. Bottom: Decomposition of $CaCO_3$. Symbols: Glass transition (☼), crystallization (❄), melting (♦). Sintering onset (❖) densification (◆), and foaming onset temperatures (❍) are taken from Figure 2. See Table 1 for sample and temperature data

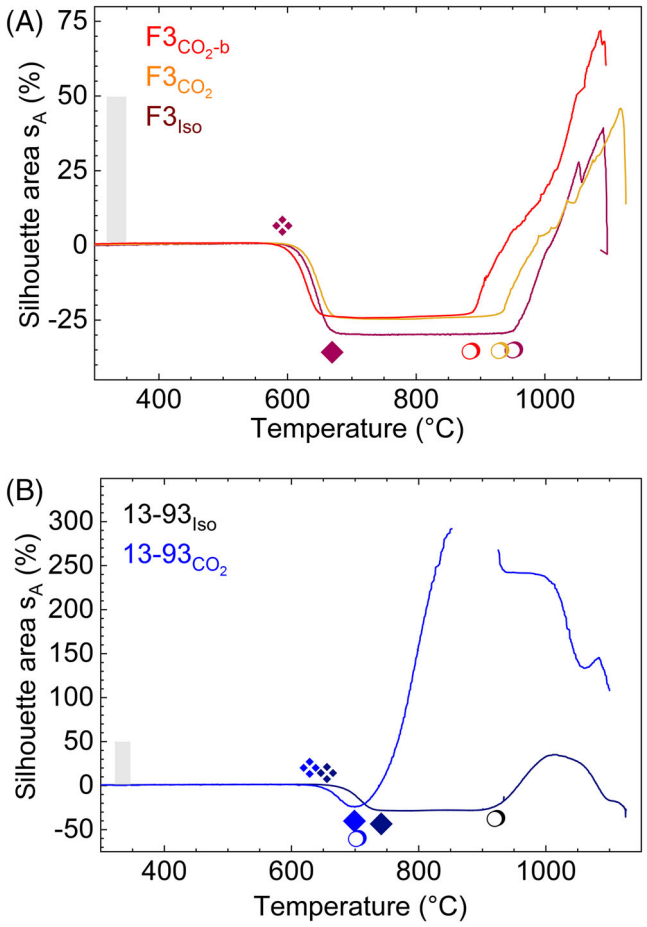

FIGURE 2 Silhouette area change, s_A, during heating at 10 K/min for F3 (A) and 13–93 (B) glass powder compacts determined via heating microscopy. Subscripts: $_{Iso}$ = 10-min milling in isopropanol, CO_2 = 1 h milling in CO_2, $_{CO_{2-b}}$ = 2-h milling in CO_2. The s_A maximum of $13–93_{CO_{2-b}}$ could not be measured.

FTIR-analysis, samples were crushed in a steel mortar and milled twice for 30 s in an agate ball mill (KM1; Janetzki, VEB Spezialmaschinenbau, Lutherstadt Wittenberg, Germany) with intensity 4. The milled samples were <20 h stored in dry air in a desiccator before the measurement, to prevent further CO_2 uptake.

Gas release was studied with vacuum hot extraction VHE (custom-made device) allowing to detect gaseous species released from powder during heating at 10 K/min ($\Delta T \approx \pm 10$ K) under a vacuum of 10^{-6} mbar via mass spectroscopy (QMA 4005, Balzers Instruments, Lichtenstein, Germany).

Time-of-flight secondary ion mass spectrometry (ToF-SIMS) was done with a ToF-SIMS^5−100 instrument (Iontof GmbH, Münster, Germany) at 2×10^{-9} mbar in high-current bunched mode. 25-keV Bi_1^+ ions (cycle time 100 μm) were used for the analysis of an area of $100 \times 100\ \mu m^2$. Depth profiling was made on 2-mm glass particles 1-h dry milled in 1-atm CO_2 before. Sputtering was made with 2 keV Cs^+ ions (≈25 nm/min at an area of $300 \times 300\ \mu m^2$). Sputter depth was calculated from process time using the Yamamura equation.

3 | RESULTS

3.1 | DTA

Figure 1 shows DTA curves for F3 and 13–93 glass powders as well as for the $CaCO_3$ raw material used in the present study. Symbols indicate characteristic temperatures attributed to glass transition (☼), crystallization (❄), and crystal melting (♦). Table 1 lists these temperatures and sample preparation data.

F3 crystallization (❄) and melting peaks (♦) confirm DTA peaks in Refs. [22, 24], which were attributed to combeite and silicorhenanite.[22,24] More detailed studies and diffraction analyses on the crystallization behavior of $F3_{Iso}$ can be found in Ref. [24]. The shoulder between 600 and 700°C for F3 milled in isopropanol ($F3_{Iso}$) is caused by sintering as indicated by the sintering (❖) and densification (◆) temperatures taken from Figure 2. The weak DTA effects above 900°C, seen for all F3 powders, might be due to foaming as indicated by its onset temperature (❍) taken from Figure 2.

The DTA curve for 13–93 milled in isopropanol ($13–93_{Iso}$) also shows a weak shoulder during sintering. The first exothermic peak at ≈1000°C occurs above the foaming onset (❍). As foaming can affect the local temperature distribution, and only a weak crystallization tendency is

TABLE 1 Sample preparation, property, and characteristic temperature data

	Symbol	$F3_{Iso}$	$F3_{CO_2}$	$F3_{CO_2-b}$	$13–93_{Iso}$	$13–93_{CO_2}$
Glass		F3	F3	F3	13–93	13–93
Milling medium		Iso	CO_2	CO_2	Iso	CO_2
Milling duration		10	60	120	10	60
Particle size	D_{10}	2	2	1	2	1
	D_{50}	11	9	4	9	4
	D_{90}	29	39	27	27	32
Glass transition	T_g ☼	540	537	537	586	592
Sintering onset	T_{S0} ❖	594	589	567	652	630
Densification	T_{SE} ◆	676	675	671	735	697
Crystallization onset	T_{C0}	685	683	681	#	#
Crystallization peaks	T_{C1} ❄	711	703	699	#	#
	T_{C2} ❄	745	739	725	#	#
	T_{C3} ❄	816	780	791	#	#
Foaming onset	T_{F0} ❍	950	933	880	900	705
Melting peaks	T_{M1} ♦	1111	1127	1074	1113	1125
	T_{M2} ♦	1160	1178	1190	–	–
Initial relative density	ρ_0	56.1	59.6	60.0	55.8	59.1
Final relative density	ρ_E	99.4	90.6	92.8	94.5	90.2

Note: Milling duration is presented in min, T in °C, D in μm, relative density in %. Iso = isopropanol. Peak temperature symbols are used in Figures 1 and 2. # = broad exothermic peaks for 13–93 above 760°C, which cannot be unambiguously attributed to crystallization.

known for 13–93, this peak could be entirely caused by foaming. The exothermic peaks between 750 and 1050°C for 13–93 milled in CO_2 (*13-93CO₂*) could be interpreted this way either. The DTA curve for $CaCO_3$ shows that the temperature range of thermal decomposition is well below the onset temperature of foaming in most cases.

3.2 | Heating microscopy

Figure 2 shows the sintering and foaming of glass powder compacts during heating in terms of the sample silhouette area change, s_A. Its decrease by 20%–25% indicates pronounced sintering. Consistently, relative densities of approximately 95% and 92% were found after sintering for milling in isopropanol and CO_2, respectively.

F3 compacts start shrinking at similar temperatures (❖, ≈600°C) due to their similar particle size (Table 1). Their foaming onset temperature (❍) decreases from ≈950 to 880°C in the order of $F3_{Iso}$, $F3_{CO_2}$, and $F3_{CO_2-b}$. As shown in Figure 3, compact size and shape remain stable up to the foaming onset for all these cases. This makes sense as pronounced crystallization occurs at ≳700°C (Figure 1). Above 880–950°C, F3 compacts foam up to $\Delta s_A \approx 70\%–90\%$ and marked spikes >1050°C indicate the bursting of large gas bubbles. Above 1090°C, s_A sharply drops as the sample volume collapses by accelerated bubble bursting and viscous flow above crystal melting. This behavior results from the low viscosity during this crystallization-retarded late foaming.

$13–93_{Iso}$ compacts show smoother foaming curves. For milling in CO_2, foaming is much more intensive ($\Delta s_A > 300\%$) and starts immediately after densification (≈700°C) whereas foaming is less intensive for milling in isopropanol ($\Delta s_A \approx 65\%$) and starts at ≈900°C.

Figure 3 also illustrates the evolution of sample color. The white color of the "green" $F3_{Iso}$ powder compacts turns to gray after densification at 668°C (Figure 2), getting darker and reaches maximum darkening at ≈800°C. Above 800°C, it lightens up and turns into yellowish gray during foaming and melting. Similar trends are evident for the $13–93_{Iso}$ compacts. The sample color turns to almost black at ≈750°C, beyond which it lightens to yellowish gray during foaming. In contrast, much less darkening was observed for the powders milled in CO_2 as exemplarily illustrated by the two fully densified samples.

3.3 | Microstructure

Figure 4 shows ESEM micrographs of $F3_{Iso}$ and $13–93_{Iso}$ glass powder compacts heated to different temperatures, quenched in air, and fractured. After sintering ($F3_{Iso}$ 670°C and $13–93_{Iso}$ 740°C), both compacts appear fully densified bearing some isolated pores. The pores are perfectly rounded for $13–93_{Iso}$ and more irregularly shaped

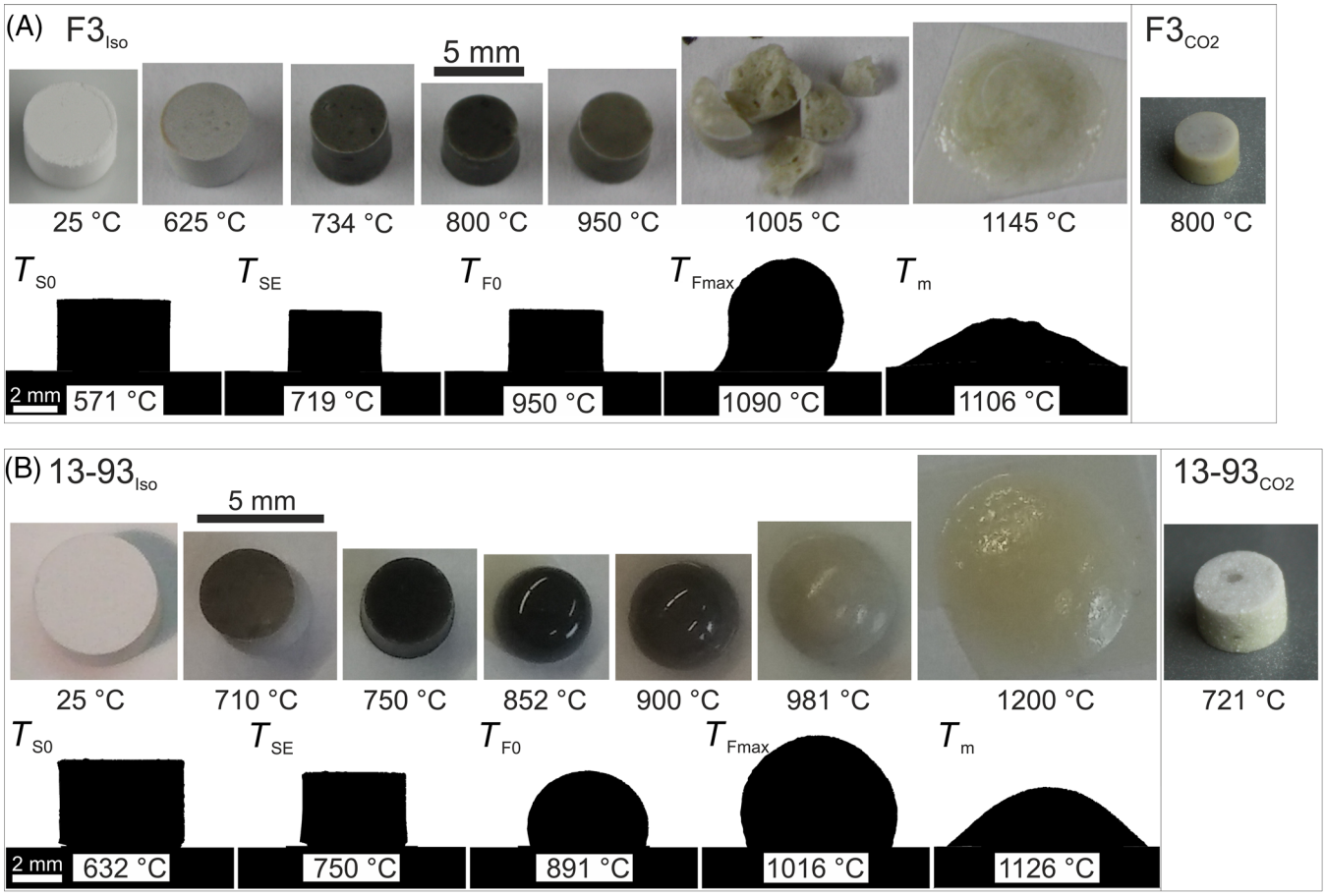

FIGURE 3 Photographs and silhouettes of F3 (A) and 13-93 (B) powder compacts heated at 10 K/min to characteristic temperatures in heating microscope and quenched in air (T_{S0} = sintering onset, T_{SE} = maximum densification, T_{F0} = foaming onset, T_{Fmax} = foaming maximum, T_m = crystal melting) powder compacts heated at 10 K/min to characteristic temperatures in heating microscope and quenched in air (T_{S0} = sintering onset, T_{SE} = maximum densification, T_{F0} = foaming onset, T_{Fmax} = foaming maximum, T_m = crystal melting)

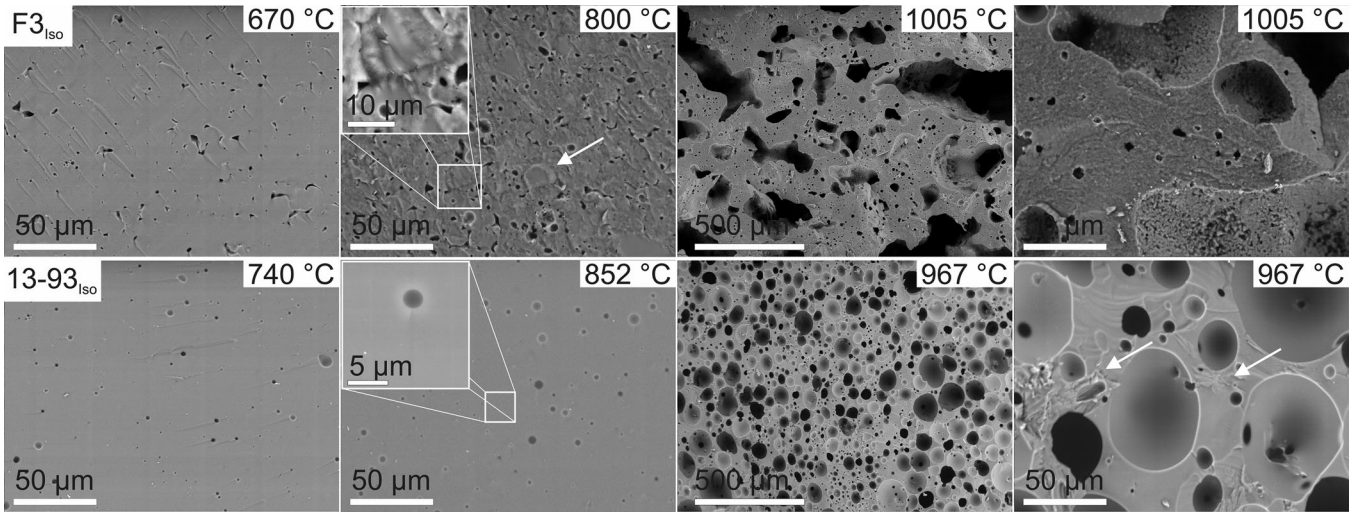

FIGURE 4 Environmental scanning electron microscopy (ESEM) micrographs of $F3_{Iso}$ (top) and $13–93_{Iso}$ (bottom) powder compacts, heated at 10 K/min to different temperatures, quenched in air, and fractured

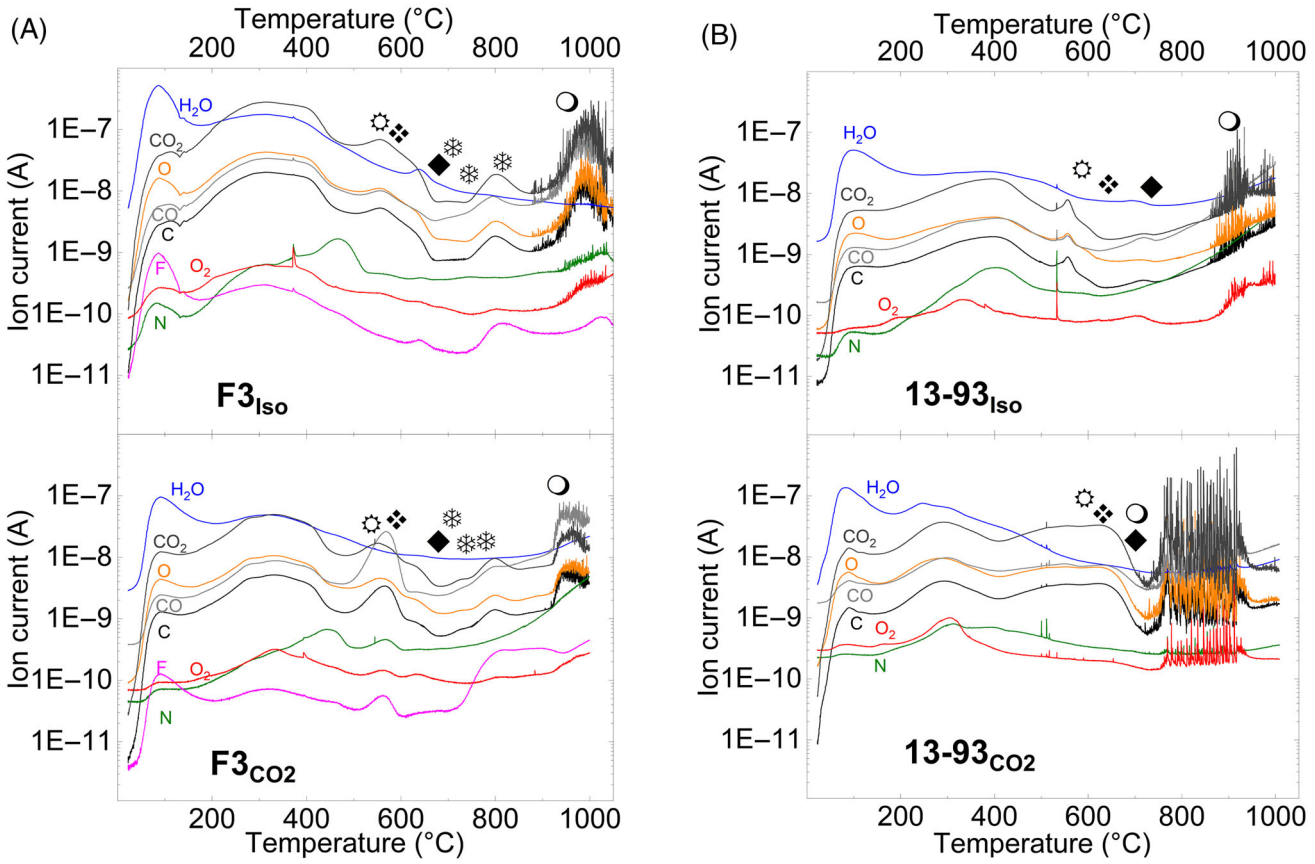

FIGURE 5 Vacuum hot extraction (VHE) degassing curves for differently milled F3 (A) and 13–93 (B) glass powders during heating at 10 K/min. $F3_{CO_2}$ and $13–93_{CO_2}$: 1-h milling in CO_2. $F3_{Iso}$ and $13–93_{Iso}$: 10-min milling in isopropanol. Characteristic temperatures derived from other figures (glass transition: ☼, sintering onset: ❖, densification: ◆, crystallization peak: ❄, foaming onset: ❍) are shown for comparison (see Figures 1 and 2).

for $F3_{Iso}$. The micrographs $F3_{Iso}$ 800°C and $13–93_{Iso}$ 852°C illustrate the compact microstructure prior to the onset of foaming. The microstructure of $F3_{Iso}$ at 800°C confirms Figure 1 as it clearly indicates the presence of crystals. These crystals grow inwards from the surface of former glass particles (arrow, inbox). In contrast, no crystals appear in the $13\text{-}93_{Iso}$ compact heated to 852°C. The micrographs $F3_{Iso}$ 1005°C and $13–93_{Iso}$ 967°C and their right neighbored detail images illustrate the microstructure evolution beyond the onset of foaming. For $F3_{Iso}$, pore size and number density are strongly increased. The fine-grained texture (detail image) indicates the presence of small crystals. $13–93_{Iso}$ compacts heated to 967°C also reveal significant increase in porosity, pores are more regularly distributed and less coagulated and only few crystals are evident (arrows).

3.4 | Degassing

The degassing behavior of glass powder compacts during heating is presented by Figure 5. Characteristic temperatures derived from other figures are shown for comparison (symbols, Table 1).

Broad peaks between 150 and 500°C can be attributed to the desorption of surface species.[28] Consistent with Refs. [12, 21], this degassing range is dominated by water and carbon gases, which most likely represent cracking fragments of carbonaceous surface species as, for example, carbonates or carboxylates.[14–16,29] As no sintering occurs in this temperature range, these species can easily escape through the open compact porosity not being able to drive later foaming. A partial degassing exhaustion of such thermally less stable surface species is indicated by the decrease in degassing between 450 and 500°C for both glasses and milling conditions.

The desorption of thermally more stable surface species is later retarded by sintering (❖–◆) as densification reduces the powder surface and increases the diffusion path lengths. This effect is most striking for carbon gases, which indicates their possible role as the major source of foaming.

After densification, a smooth degassing peak at 800°C appears for F3. As expected from the sinter-induced drop

in their degassing activity, this mechanism is driven by carbon species. As this degassing temperature is well above T_g, the compact is fully densified, and no degassing spikes indicate bursting gas bubbles, this degassing should reflect the outward diffusion of carbon species from the compact bulk. It is difficult, however, to understand why such outward diffusion exhausts prior to foaming. A speculative explanation could be related to the striking degassing of fluor. As its degassing temperature range correlates with the late stage of F3 crystallization, and flour is not incorporated into the crystal phase,[24] fluor could be enriched in the residual glass phase as recently shown for CaO–MgO–Al_2O_3–SiO_2 glass–ceramics.[30] This effect could locally decrease glass viscosity,[31] which finally would increase diffusion-limited degassing. As this effect would be limited to the surface near a region of former glass particles, which undergo surface crystallization, and fluor would finally get depleted and increase viscosity again, a temporary degassing exhaust might be understandable.

At high temperatures, degassing strongly increases at the onset of foaming (❍), where sharp spikes indicate bursting gas bubbles. As this degassing range reveals the major foaming source, Figure 5 clearly proves that foaming is driven by carbon gases. Figure 5 also shows that this degassing strongly depends on powder processing. For *13–93*$_{CO_2}$, foaming starts right after densification at ≈700°C, whereas foaming is much less intensive and starts at ≈850°C for *13–93*$_{Iso}$. This finding gives clear evidence, that the foaming source is related to carbon species trapped at the powder surface.

3.5 | FTIR

To get hints into the possible nature of such carbonaceous surface species, all powders were studied with ATR-FTIR spectroscopy. Figure 6 shows double bands in the range 1350–1580 cm^{-1}, which correspond to typical asymmetric stretching vibrations of carbonates. For 13–93, a center position of 1470 cm^{-1} and $\Delta\nu_{as} \approx 120$ cm^{-1} occurs (upper arrows). The peak intensity does not significantly vary for milling in isopropanol and CO_2 but decreases after heating to 740°C. A center position of ≈1450 cm^{-1} and $\Delta\nu_{as} \approx 75$ cm^{-1} occurs for all F3 milling regimes (lower arrows). The doublet peak is less intensive for milling in isopropanol and it significantly decreases after heating. The carbonate doublet is most pronounced for 2-h milling in CO_2. Consistent with Figures 2 and 5, this finding indicates that carbonates have been enriched during milling in CO_2. The doublet intensity again decreases after heating, but this effect is less pronounced.

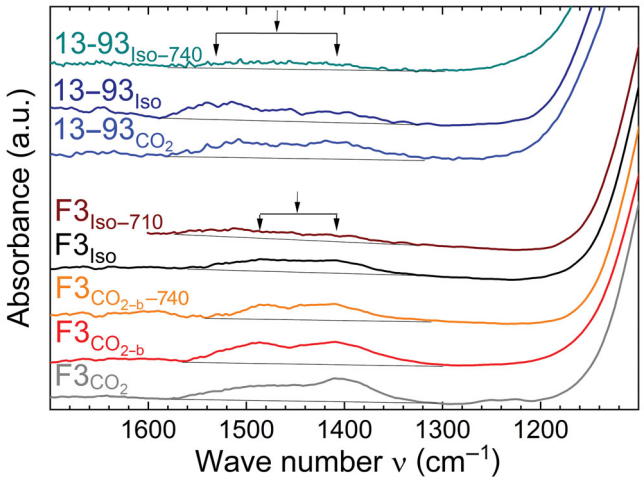

FIGURE 6 ATR-FTIR absorbance spectra of differently milled glass powders. For F3 2-h milled in CO_2 ($F3_{CO_{2-b}}$), ATR-FTIR measurements were performed before and after heating at 10 K/min to 740°C in air. Absorbance is normalized to the Si–O stretching band at 930 cm^{-1}. Arrows indicate average doublet center position and splitting of the carbonate doublet.

3.6 | ToF-SIMS

Surface near carbonaceous species could also be revealed by depth profiling with ToF-SIMS. Due to the analyzed area of 100 × 100 μm^2, however, the measurement was made on 2-mm F3 glass particles exposed to 1-h milling in CO_2 prior to the measurement.

Figure 7A shows the depth profile measured for this particle. As expected, most frequent species are correlated with major glass components and do not show any surface near concentration enrichment. Although carbonates were clearly detected in Figure 6, no surface near enrichment is evident for carbonates or possibly related fragments. Unfortunately, the carbonate ion itself, however, cannot be detected in the present case because of similar mass numbers for SiO_2 (60.084) and CO_3 (60.009). The only possible fragment could be C for which a surface near enrichment is clearly detectable. As shown in Figure 7B, this enrichment is not evident for the fractured sample, whereas it still occurs for the glass particle exposed to milling and heated to 520°C. This annealing treatment should make sure that weakly trapped species, which would not cause later foaming, are fully desorbed prior to measurement.

On the other hand, the surface near carbon enrichment observed in Figure 7 could also reveal adventitious carbon environmental contaminations as indicated by the depth profiles of chlorine and sulfur. The mechanically rough surface of milling exposed particles (see e.g., Ref. [21]) and the large, analyzed surface area could pretend an extended depth profile for surface contaminants.

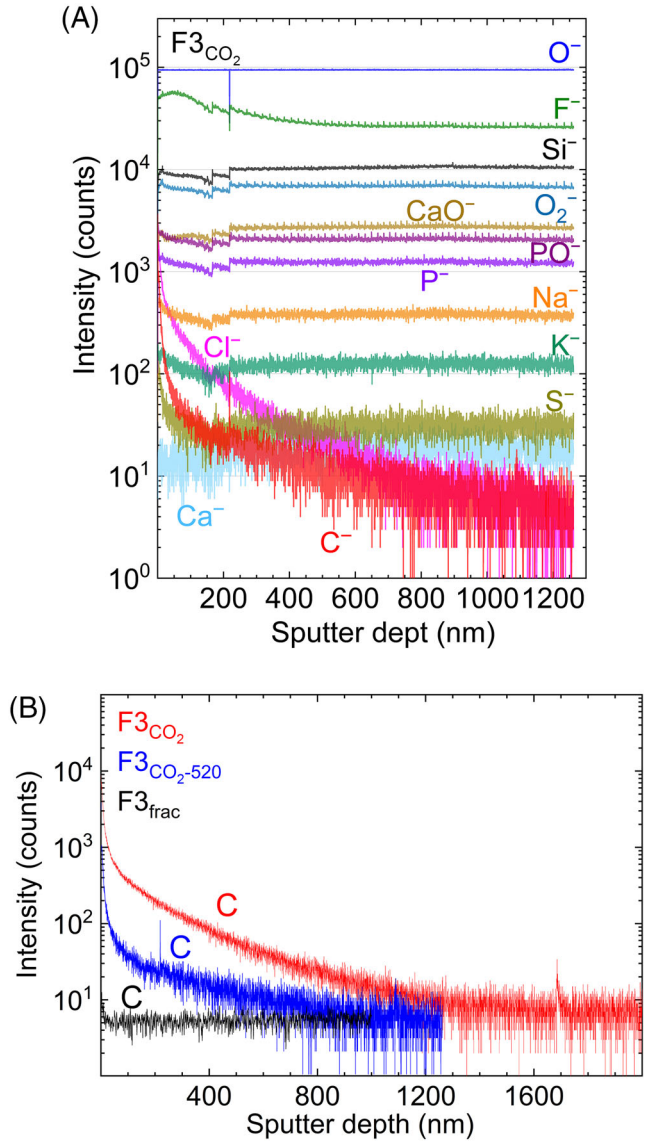

FIGURE 7 (A) Time-of-flight secondary ion mass spectrometry (ToF-SIMS) depth profiles measured at the surface of a 2-mm glass particle exposed to 1-h milling in CO_2 prior to the measurement. (B) Carbon depth profiles at a freshly fractured surface ($F3_{frac}$), and at glass particles exposed to 1-h milling in CO_2 before ($F3_{CO_2}$) and after heating to 520°C at 10 K/min ($F3_{CO_{2-520}}$)

4 | DISCUSSION

Carbon gases provide the major blowing agents for both glasses under study. This conclusion is proved by Figure 2 showing that bursting gas bubbles, indicated by sharp degassing spikes occurring during foaming, predominantly release carbon gases. This finding is consistent with similar observations for a barium alumino-borosilicate glass (*K01*) reported in Refs. [12, 21].

In contrast, water does not contribute to foaming as indicated by the absence of degassing spikes in the temperature range of foaming. The same effect was found in Refs. [12, 21]. Although water dominates degassing at low temperature in all cases, it obviously tends to fully escape before being encapsulated during densification. Figure 2 also indicates minor foaming contributions of oxygen and nitrogen. But, as newly formed gas bubbles may serve as diffusion sinks (as utilized in glass fining), this is most likely due to secondary transport kinetic phenomena.

The present study also shows that the *carbonaceous species*, from which carbon gases later emerge, must be *trapped at or close beneath the surface*. This is indicated by the strong effect of milling on degassing intensity in Figure 2. The same conclusion for the glass *K01* was made in Refs. [12, 21] based on the strong effect of milling duration, milling atmosphere, and powder storage on later foaming.

4.1 | Carbonates

4.1.1 | Adsorbed carbonates

As a simple and intuitive idea, *adsorbed carbonates* could be assumed to provide the major foaming source. Their presence, however, could not be proved by IR spectroscopy for the barium alumino-borosilicate glass *K01* studied in Ref. [21] as the carbonate doublet at ≈1350–1580 cm^{-1} overlaps with a strong BO_3 glass band at ≈1440 cm^{-1}. For the not boron-containing bioactive glasses under the present study, however, the ATR-FTIR spectra in Figure 6 clearly prove the occurrence of carbonate doublets.

Moreover, comparing the onset temperatures of foaming in Figure 2 with the temperature range of $CaCO_3$ decomposition in Figure 1 gives clear evidence that $CaCO_3$ starts to decompose well below the onset of foaming and could therefore provide the major foaming source. The $CaCO_3$ decomposition temperature range was even lowered by $\Delta T \approx 70$ K after mix-milling with F3 glass powder.[32] Thus, even the low foaming onset of the $13–93_{CO_2}$ glass powder does not question the suitability of $CaCO_3$ as a major foaming source.

4.1.2 | Mechanically entrapped carbonates

As another important prerequisite, foaming sources must not escape during heating to the temperature of sintering. XPS and ToF-SIMS studies on *K01* in Ref. [21], however, failed to prove the existence of *carbonates* at the surface of glass powders after heating to the sintering onset temperature. Instead, several findings in Ref. [21] suggest that carbonates can be *entrapped* close beneath the surface due to the strong mechanical surface damage during milling.

Such mechanisms were previously discussed for milling crystalline substances.[17,19]

The present study provides some hints on such a mechanical trapping mechanism. The first one is seen in Figure 6, in which carbonate doublets are evident even for samples heated to 740°C. Although the $CaCO_3$ decomposition curve in Figure 1 stretches up to 800°C, this high temperature represents the decomposition kinetics rather than the decomposition temperature threshold. This threshold temperature is indicated to be ≈600–650°C and could be even lowered by mechanical damaging during milling as shown in Ref [32]. As the carbonate doublet would disappear above this threshold temperature range without any kinetic retardation, its thermal stability up to 740°C in Figure 6 would be better understandable assuming a mechanical trapping mechanism.

Consistent with such a trapping mechanism, VHE studies in on *K01*[21] revealed smooth diffusion-limited degassing peaks at $\approx T_g$. Their diffusive nature was indicated as they involve the degassing of argon for the powder intensively milled in this atmosphere. This observation hints on the diffusion-limited degassing of argon as argon adsorbed to the powder surface should fully escape during heating to T_g. In the present case, mechanically entrapped carbonates are indicated by the degassing behavior of F3. In this case, the smooth degassing peak at $\approx T_g$, which is mainly driven by carbon gases, also includes the degassing of fluor, which is part of the glass composition. This effect is not only more pronounced for F3 milled in CO_2 but also occurs for milling in isopropanol. The minor contribution of nitrogen and oxygen to the smooth degassing peak at $\approx T_g$ makes also sense as they should have been encapsulated in tight agglomerates during heating to T_g. This effect is more pronounced for $F3_{CO_2}$ as for this intensive dry milling large agglomerate formation tendency is expected and is in fact indicated by smaller D_{50} and larger D_{90} values (Table 1).

4.2 | Residual carbon

Another source of carbon gas could be *residual carbon*. This mechanism is indicated by the gray color evolution for 13–93 and F3 milled in isopropanol (Figure 3). For both glasses, maximum darkening appears well above the densification temperature and the gray color progressively disappears during foaming. Both observations suggest that residual carbon is stable enough to be trapped during heating to the densification temperature and that oxidation to carbon gases occurs during foaming. In contrast, such color evolution was not found for milling in CO_2.

Residual carbon is well known to occur in ceramic processing when organic aids are not fully removed before sintering. As viscous sintering of glass powders can proceed at low temperatures, this effect might occur even if only traces of residual organics are expected. Thus, Eqtesadi et al.[33] found a similar black coloration for 13–93 powder sintered at 700°C and attributed it to residual carbon from milling in anhydrous ethanol. Due to the high solubility of bioactive glasses, water-free milling was also applied in the present case.

The idea that the observed oxidation of carbon during foaming between 900 and 1200°C is driven by the inward diffusion of atmospheric oxygen diffusion, however, is difficult due to its low diffusion coefficient. Thus, even for molecular oxygen diffusion at 1000°C very low diffusion coefficients should occur. Schaeffer[34] reported O_2 diffusion coefficients of $D_{O_2} = 10^{-9}$ cm^2/s for the glass $16Na_2O–12CaO–72SiO_2$[35] and $\approx 10^{-5}$ cm^2/s for the glass $40CaO–20Al_2O_3–40SiO_2$.[36] This way, diffusion lengths of $(D_{O_2} \cdot 1\ h)^{1/2} = 2000–18\ \mu m$ would result after 1-h annealing. This rough estimation shows that oxygen inward diffusion during heating is most likely limited to the outermost compact surface near region, whereas gas bubble formation obviously occurs throughout the whole compact volume (Figure 3).

Another oxygen source could be the thermal decomposition of carbonates. Although residual carbon should be oxidized to CO_2 at room temperature, the Boudouard equilibrium $CO_2 + C \rightleftharpoons 2CO$ is approached for the given temperature. As an example, this equilibrium is $k_{CO_2/CO} \approx 3/97$ at 900°C and 1 bar.[37] Thus, it could be assumed that CO_2 released from decomposed carbonate partially decomposes to CO and thereby oxidizes residual carbon to CO. This way, residual carbon may contribute to foaming. This hypothesis allows one to explain the homogeneous distribution of color and gas bubbles during foaming (F3 1005°C) in Figure 3. The strong difference in the foaming onset temperatures for milling 13–93 in isopropanol and CO_2 seen in Figure 2 may be explained analogously. As both powders are similar in size and the same viscosity and crystallization tendency can be expected, this difference should be related to differently abundant foaming sources. As carbonates are required both for the foaming directly caused by carbonate decomposition and indirectly via oxidizing residual carbon, their abundance is a key limiter of foaming. This way, the late foaming onset of 13–93 compacts for milling in isopropanol could result from less abundant carbonates as actually indicated by Figure 6. On the other hand, this explanation and the simultaneous occurrence of foaming and color change seen in Figure 3 cannot prove that foaming is essentially driven by residual carbon oxidation at all. This oxidation could be a side effect

of carbonate decomposition and not essentially contribute to foaming.

5 | SUMMARY

Both bioactive glasses under study, F3 and 13–93, undergo pronounced foaming. Foaming onset temperatures and intensity, however, strongly depend on glass crystallization and milling conditions.

Consistent with previous studies, VHE degassing measurements prove c*arbon gases* to provide the major foaming agents for both glasses and milling conditions under study, whereas water does not essentially contribute. The strong effect of milling conditions on foaming shows that the *carbonaceous species*, from which carbon gases later emerge, must be *trapped at or at least close beneath the particle surface*. ATR-IR spectra of F3 and 13–93 glass powders clearly prove the presence of typical carbonate doublets even after heating to sintering temperatures. Surface carbonates can therefore be regarded as the major foaming source in the present case.

Consistent with Ref. [21], our study indicates the occurrence of *mechanically trapped carbonates*. Assuming that the thermal stability of surface carbonates is the primary trapping mechanism, could not explain why carbonate doublets are detectable even after heating to 740°C, whereas DTA curves indicate thermal $CaCO_3$ decomposition threshold temperatures at ≈600–650°C. Mechanical trapping or encapsulation of surface carbonate would also explain the smooth degassing peak at $\approx T_g$, which is mainly driven by carbon gases, but likewise includes the quite similar degassing of fluor, which is part of the glass composition. This mechanism might also explain why carbonates are most abundant for 2-h (dry) milling in CO_2. For this milling condition, maximum mechanical damage can be expected, whereas the opposite should be expected for (wet) milling in isopropanol.

For milling in isopropanol, the observed color evolution of glass powder compacts during heating, sintering, and foaming indicates *residual carbon* as a possible second foaming source. The observed color change from dark gray to light yellow during foaming, however, cannot exclude that residual carbon oxidation is just a side effect and does not necessarily contribute essentially to foaming. Due to limited inward diffusion of ambient oxygen, the most propel oxygen source is carbonate, as CO_2, which is released after carbonate decomposition, can partially react with residual carbon to form CO according to Boudouard's equilibrium.

As carbonates are required both for the foaming directly caused by carbonate decomposition and indirectly via oxidizing residual carbon, their abundance is a key limiter of foaming. The strong difference in foaming intensity and onset temperature for 13–93 glass powder compacts milled in CO_2 and isopropanol can be explained this way.

The strong foaming retardation for milling F3 in CO_2 compared to milling 13–93 in CO_2 can be attributed to glass crystallization. As the presence of crystals increases the compact effective viscosity, higher temperatures are needed to allow the formation and growth of gas bubbles. In contrast, foaming is not retarded by crystallization for the glass 13–93.

ACKNOWLEDGMENTS

We are grateful to acknowledge the experimental support by S. Gierth from the Fraunhofer Institute for Microstructure of Materials and Systems IMWS for ToF-SIMS measurements and our colleagues from BAM I. Feldmann for ESEM imaging and S. Reinsch for VHE measurements. Financial support by the Deutsche Forschungsgemeinschaft DFG (Mu963 18-1) is gratefully acknowledged as well.

Open access funding enabled and organized by Projekt DEAL.

REFERENCES

1. Suvorova OV, Makarov DV. Foam glass and foam materials based on ash-slag wastes from thermal power plants (review). Glass Ceram. 2019;76(5–6):188–93.
2. Bernardo E, Elsayed H, Romero AR, Crovace MC, Zanotto ED, Fey T. Biosilicate® glass–ceramic foams from refined alkali activation and gel casting. Front Mater. 2021;7:11.
3. Konig J, Petersen RR, Iversen N, Yue YZ. Application of foaming agent-oxidizing agent couples to foamed-glass formation. J Non-Cryst Solids. 2021;553:120469.
4. Zhang JJ, Liu B, Zhang SE. A review of glass ceramic foams prepared from solid wastes: processing, heavy-metal solidification and volatilization, applications. Sci Total Environ. 2021;781:146727.
5. Jordanov NB, Georgiev I, Karamanov A. Sintered glass–ceramics, self-glazed materials and foams from metallurgical waste slag. Materials. 2021;14(9):2263.
6. Lucchini E, Meriani S, Slokar G. Sintering of glass bonded ceramic barium hexaferrite magnetic powders. J Mater Sci. 1983;18(5):1331–4.
7. Leonelli C, Bondioli F, Veronesi P, Romagnoli M, Manfredini T, Pellacani GC, et al. Enhancing the mechanical properties of porcelain stoneware tiles: a microstructural approach. J Eur Ceram Soc. 2001;21(6):785–93.
8. Hwang GH, Jeon HJ, Kim YS. Physical properties of barrier ribs of plasma display panels: I, formation of pores during sintering of lead borosilicate glass frits. J Am Ceram Soc. 2002;85(12):2956–60.
9. Lara C, Pascual MJ, Prado MO, Duran A. Sintering of glasses in the system RO-Al_2O_3–BaO-SiO_2 (R = Ca, Mg, Zn) studied by hot-stage microscopy. Solid State Ionics. 2004;170(3–4):201–8.
10. Lim ES, Kim BS, Lee JH, Kim JJ. Effect of BaO content on the sintering and physical properties of BaO–B_2O_3–SiO_2 glasses. J Non-Cryst Solids. 2006;352(8):821–6.

11. Muller R, Meszaros R, Peplinski B, Reinsch S, Eberstein M, Schiller WA, et al. Dissolution of alumina, sintering, and crystallization in glass ceramic composites for LTCC. J Am Ceram Soc. 2009;92(8):1703–8.
12. Agea-Blanco B, Reinsch S, Müller R. Sintering and foaming of barium silicate glass powder compacts. Front Mater. 2016;3:10.
13. Baptist R, Levy F. Carbon-dioxide adsorption on glass. Vacuum. 1992;43(3):213–4.
14. Cerruti M, Morterra C. Carbonate formation on bioactive glasses. Langmuir. 2004;20(15):6382–8.
15. Seiferth O, Wolter K, Dillmann B, Klivenyi G, Freund HJ, Scarano D, et al. IR investigations of CO_2 adsorption on chromia surfaces: Cr_2O_3 (0001)/Cr(110) versus polycrystalline alpha-Cr_2O_3. Surf Sci. 1999;421(1–2):176–90.
16. Li C, Sakata Y, Arai T, Domen K, Maruya K, Onishi T. Carbon-monoxide and carbon-dioxide adsorption on cerium oxide studied by Fourier-transform infrared-spectroscopy . Formation of carbonate species on dehydroxylated Ceo2 at room-temperature. J Chem Soc Farad Trans 1. 1989;85:929–43.
17. Kalinkina EV, Kalinkin AM, Forsling W, Makarov VN. Sorption of atmospheric carbon dioxide and structural changes of Ca and Mg silicate minerals during grinding – II. Enstatite, akermanite and wollastonite. Int J Miner Process. 2001;61(4):289–99.
18. Kalinkina EV, Kalinkin AM, Forsling W, Makarov VN. Sorption of atmospheric carbon dioxide and structural changes of Ca and Mg silicate minerals during grinding – I. Diopside. Int J Miner Process. 2001;61(4):273–88.
19. Kalinkin AM, Kalinkina EV. The mechanosorption of carbon dioxide by magnesium, calcium, and strontium metasilicates. Russ J Phys Chem. 2010;84(9):1585–91.
20. Heinicke G, Hennig HP, Linke E, Steinike U, Thiessen KP, Meyer K. Tribochemistry. Berlin: Akademie-Verlag; 1984. p. 495
21. Muller R, Behrens H, Agea-Blanco B, Reinsch S, Wirth T. Foaming species and trapping mechanisms in barium silicate glass sealants. Adv Eng Mater. 2022;24(6):2100445
22. Groh D, Doehler F, Brauer DS. Bioactive glasses with improved processing. Part 1. Thermal properties, ion release and apatite formation. Acta Biomater. 2014;10(10):4465–73.
23. Doehler F, Groh D, Chiba S, Bierlich J, Kobelke J, Brauer DS. Bioactive glasses with improved processing. Part 2. Viscosity and fibre drawing. J Non-Cryst Solids. 2016;432:130–6.
24. Blaeß C, Müller R, Poologasundarampillai G, Brauer DS. Sintering and concomitant crystallization of bioactive glasses. Int J Appl Glass Sci. 2019;10(4):449–62.
25. Pirhonen E, Niiranen H, Niemelä T, Brink M, Törmälä P. Manufacturing, mechanical characterization, and in vitro performance of bioactive glass 13–93 fibers. J Biomed Mater Res B Appl Biomater. 2006;77B(2):227–33.
26. Coon E, Whittier AM, Abel BM, Stapleton EL, Miller R, Fu Q. Viscosity and crystallization of bioactive glasses from 45S5 to 13–93. Int J Appl Glass Sci. 2020;12(1):65–77.
27. Winkel A, Meszaros R, Reinsch S, Muller R, Travitzky N, Fey T, et al. Sintering of 3D-printed glass/HAp composites. J Am Ceram Soc. 2012;95(11):3387–93.
28. Muller R, Gottschling P, Gaber M. Water concentration and diffusivity in silicates obtained by vacuum extraction. Glass Sci Technol. 2005;78(2):76–89.
29. Davydov AA. Infrared spectroscopy of adsorbed species on the surface of transition metal oxides. In: Rochester CH, editor. Chichester: John Wiley & Sons Ltd; 1990. p. 258. ISBN: 0-471-91813-X.
30. Pei F, Zhu G, Li P, Guo H, Yang P. Effects of CaF2 on the sintering and crystallisation of CaO–MgO–Al_2O_3–SiO_2 glass–ceramics. Ceram Int. 2020;46(11, Part):17825–35.
31. Brauer DS, Anjum MN, Mneimne M, Wilson RM, Doweidar H, Hill RG. Fluoride-containing bioactive glass–ceramics. J Non-Cryst Solids. 2012;358(12–13):1438–42.
32. Agea Blanco B, Blaess C, Reinsch S, Brauer D, Müller R, editors. Sintering and foaming of barium and calcium silicate glass powders. In: 11th International CICMT Conference and Exhibition. Dresden: IMAPS/ACerS; 2015.
33. Eqtesadi S, Motealleh A, Pajares A, Miranda P. Effect of milling media on processing and performance of 13–93 bioactive glass scaffolds fabricated by robocasting. Ceram Int. 2015;41(1, Part B):1379–89.
34. Schaeffer HA. Sauerstoff- und Siliciumdiffusion in silicatischen Gläsern [Habilitationsschrift]. Erlangen: Friedrich-Alexander Universität Erlangen-Nürnberg; 1980.
35. Terai R, Oishi Y. Self-diffusion of oxygen in soda-lime silicate glass. Glass Sci Technol. 1976;50:68–73.
36. Sasabe M, Goto KS. Permeability, diffusivity, and solubility of oxygen gas in liquid slag. Metall Trans. 1974;5(10):2225–33.
37. Lide DR. CRC handbook of chemistry and physics. 90th ed. Boca Raton, FL: CRC Press; 2009. p. 2804

How to cite this article: Blaeß C, Müller R. Sintering and foaming of bioactive glasses. J Am Ceram Soc. 2022;1–11.
https://doi.org/10.1111/jace.18626